Geomechanics and Engineering, *Vol. 12*, *No. 1* (*2017*) *139-160*
DOI: https://doi.org/10.12989/gae.2017.12.1.139

Model test and numerical simulation on the bearing mechanism of tunnel-type anchorage

Yujie Li, Rong Luo, Qihua Zhang, Guoqiang Xiao, Liming Zhou and Yuting Zhang *

Key Laboratory of Geotechnical Mechanics and Engineering of the Ministry of Water Resources, *Yangtze River Scientific Research Institute*, *Wuhan*, *Hubei 430010*, *China*

(*Received April 23*, *2016*, *Revised September 18*, *2016*, *Accepted September 27*, *2016*)

Abstract. The bearing mechanism of tunnel-type anchorage (TTA) for suspension bridges is studied. Model tests are conducted using different shapes of plug bodies, which are circular column shape and circular truncated cone shape. The results show that the plug body of the latter shape possesses much larger bearing capacity, namely 4.48 times at elastic deformation stage and 4.54 times at failure stage compared to the former shape. Numerical simulation is then conducted to understand the mechanical and structural responses of plug body and surrounding rock mass. The mechanical parameters of the surrounding rock mass are firstly back-analyzed based on the monitoring data. The calculation laws of deformation and equivalent plastic strain show that the numerical simulation results are rational and provide subsequent mechanism analysis with an established basis. Afterwards, the bearing mechanism of TTA is studied. It is concluded that the plug body of circular truncated cone shape is able to take advantage of the material strength of the surrounding rock mass, which greatly enhances its bearing capacity. The ultimate bearing capacity of TTA, therefore, is concluded to be determined by the material strength of surrounding rock mass. Finally, recommendations for TTA design are proposed and discussed.

Keywords: tunnel-type anchorage(TTA); model test; numerical simulation; bearing mechanism; ultimate bearing capacity; design concept

1. Introduction

Currently, there are many ongoing and scheduled highway projects in western region of China. Due to the restrictions of complicated geographical, geological and climatic conditions, bridges and tunnels cover a large proportion of the highway mileage. For high mountain and deep valley regions, large bridges with single span of kilometer level are gradually emerged as a suitable alternative.

Of the many types of bridges, suspension bridge possesses favorable adaptability in different scales of span and its stiffness girder height can remain stable when the span magnitude varies, thus avoiding excessively high piers and also helping to reduce the adverse influences of bridge construction on river shipping and flood protection. It is for these reasons that suspension bridge is considered an appropriate option for mountainous regions. There are self-anchored type and ground-anchored type for suspension bridges. The ground-anchored type is further divided into

*Corresponding author, Ph.D., E-mail: magicdonkey@163.com

http://www.techno-press.org/?journal=gae&subpage=7 ISSN: 2005-307X (Print), 2092-6219 (Online)

tunnel-type anchorage (hereinafter abbreviated as TTA) and gravity-type anchorage. TTA is able to take advantage of material strength and bearing capacity of rock mass at anchoring area. So it involves much smaller amount of project quantities compared to gravity-type anchorage and is considered as a cost effective approach with less environmental disturbance. Despite the above advantages, TTA requires favorable rock mass quality and its interaction with the surrounding rock mass plays a major role in its performance.

Engineering practices show that TTA is commonly designed as a plug body with inverted cone shape. The cross section of its front face is smaller than that of its back face. The main cable force is directly imposed on the TTA and then transferred to the surrounding rock mass, causing rock mass undertake considerable pulling effect. As the surrounding rock mass has high material strength and stiffness, the anti-pulling capacity of TTA is greatly enhanced. Table 1 summarizes the main indexes of world's major suspension bridges using TTA. It is found that since the new millennium an increasing number of bridges adopt TTA and the dimensions of TTA are also becoming increasingly larger.

On one hand, current research on suspension bridges is mainly focused on their structural

Table 1 Main indexes of world's major suspension bridges using tunnel-type anchorage

Name of suspension bridges	State	Main span /m	Main cable force /MN	Size of anchorage /m		
				Front face	Back face	Length
George Washington Bridge (Ammann 1933)	USA	1066.8	550	10×12	17×20	45.7
Forth Road Bridge (Roberts *et al*. 1967)	UK	1005.8	140	7.6	10.7×13.7	77
Seto-Ohashi Bridge (Miki *et al*. 2002)	Japan	940	320	6.7×11.0	14.7×14.0	77.2
Humen Bridge: Preliminary design (Chen *et al*. 1995)	China	888	158	9×10	13×14	53
Fengdu Yangtze River Bridge (Wang and Cao 2004)	China	450	68.5	7×8	10×10	10
Egongyan Yangtze River Bridg (Lu 2003)	China	600	130	9.5×10.5	12.5×13.5	42
Wanzhou 2nd Yangtze River Bridge (Yang *et al*. 2002)	China	580	102	6×6	14×14	15
Jiaolongba Bridge (Lei 2005)	China	345	54	4×8	6×12	13
NanxiYangtz River Bridge (Min *et al*. 2011)	China	820	200	10×10	20×20	25
Balinghe River Bridge (Hu *et al*. 2007)	China	1088	270	10×10.8	21×25	40
Siduhe River Bridge (Zhu *et al*. 2006)	China	900	220	10.5×10.5	14×14	40
Aizhai Bridge (Zhang *et al*. 2012)	China	1176	310	11×12	15×16	43

response under wind or vibration (Zhang *et al*. 2013, Wang *et al*. 2015). On the other hand, the studies of anchors and their bearing mechanism are primarily referring to piles (Shen *et al*. 2013, Zhang *et al*. 2014, Hataf and Shafaghat 2015, Saleem 2015) which are used to reinforce soils or sand (Kame *et al*. 2012, Niroumand and Kassim 2013, Bildik and Laman 2015), rather than provide anti-pulling forces against external forces. Till now, methodologies and concepts regarding TTA design are neither included in current Chinese codes and regulations (The Professional Standards Compilation Group of the People's Republic of China 2002), nor reported by many literatures. For project safety concerns, only the gravity of TTA is considered as resistant force against main cable force while the remarkable resistance provided by the surrounding rock mass is not taken into account. This design concept basically treats TTA as gravity-type anchorage, inevitably leading to much larger volume of anchorage body and unnecessary higher expense. So far, theoretical basis and bearing mechanism of TTA have not been studied sufficiently. Although a number of researches have been done on bearing mechanism of TTA (Table 2), none is able to provide a whole process of mechanical and structural response of TTA under gradually increasing loads.

The "experimental plus numerical" approach has been repeatedly proved effective in studying the mechanism of new structures (Bencardino and Condello 2014, 2015, Moradi and Abbasnejad 2015, Spadea *et al* 2015, Zhu *et al*. 2014) and it is also adopted in TTA study. Firstly, to interpret the bearing mechanism of TTA and provide useful recommendations for its design, it is necessary to collect data describing responses of both TTA and surrounding rock mass from loading initiation stage to failure stage using model test approach. Therefore, the ultimate load, which is a key index to quantify the maximum anti-pulling capacity corresponding to the failure stage of TTA, can be obtained. Secondly, numerical simulation approach is also indispensable to understand the evolution of deformation, stress and probable internal failure planes of TTA and the surrounding rock mass. By combined analysis of model test data and numerical simulation results, an insight into the bearing mechanism of TTA and its interaction with the surrounding rock mass can be

Table 2 Summary of researches on mechanism of action of tunnel-type anchorage

Name	Approach	Similarity ratio	Maximum applied load	Comments
Jiaolongba Bridge (Wang *et al*. 2005)	Model test	-	-	Mainly obtained pull out strength of cables
Humen Bridge (Xia *et al*. 1997)	Model test	1:50	4.8*p*	Plastic deformation observed but no TTA failure
Egongyan Yangtze River Bridge (Xiao *et al*. 2005)	Model test	1:12.5	4.6*p*	Test aborted due to steel wire failure but no TTA failure
Balinghe River Bridge (Hu *et al*. 2007)	Model test	1:20, 1:30	1.1*p*	No TTA failure
Siduhe River Bridge (Zhu *et al*. 2006)	Model test	1:12	7.6*p*	Measured deformation is very small and no TTA failure
Aizhai Bridge (Zhang *et al*. 2012)	Numerical simulation	-	7*p*	No model test results

Note: the "*p*" in the "Maximum applied load" column refers to the design load against the main cable force achieved. Based on above understanding, and with the attempts to evaluate TTA performance and recommend its design concept, both model test and numerical simulation are conducted.

2. Model test of TTA#

2.1 Project overview

The studied project is a large scale suspension bridge and plans to use TTA to provide resistance against main cable force. The bridge deck width is 24.5 m. It is 964 m long and its main span is 628 m long. The design load of main cable force is 2×101.341 MN. The bridge adopts TTA at one side and gravity-type anchorage at the other side. The angle of inclination of main cable force is 40°. The spacing between the two main cables is 26.0 m. The plug body is 35.0 m long and its cross section is half-circular-half-rectangular type with top arch radius of 4.75 m on front face and 6.50 m on back face. The height and width is both 9.5 m for front face of plug body and both 13.0 m for its back face.

2.2 Model test preparations

As exploratory tunnels have been excavated in the scheduled TTA region, two branch openings parallel to each other are further excavated for model test purpose in one of the exploratory tunnels. Hence, the rock wall between parallel openings are chosen as model test area. (9# branch opening and 10# branch opening in Fig. 1) Geological exploration reveals that the rock mass is mainly limestone with thick-layered structure. The spacing of major fractures is about 3~50 cm and the fractures are mostly closed. Corrosion are found along fractures and calcites are filled in a small proportion of fractures. It is evaluated that the surrounding rock mass at both top arch and side wall area are stable. Before model test, geophysical measurements are conducted and show that the velocity of longitudinal wave of surrounding rock mass at model test area ranges from 2900 m/s to 3900 m/s. The intactness index of rock mass is 0.37 according to Chinese national standard for rock mass classification (The Professional Standards Compilation Group of the People's Republic of China 2015). Therefore, the rock mass is considered as moderately fractured.

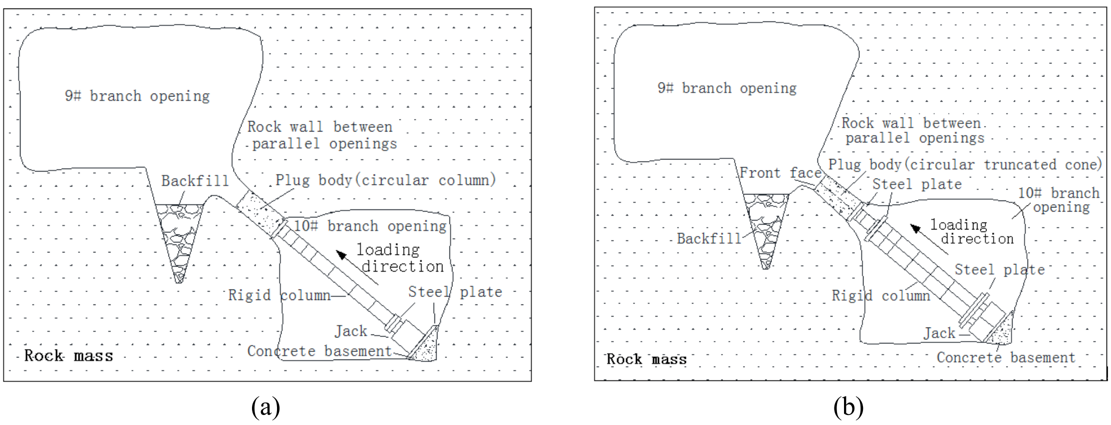

Fig. 1 Cross-sectional profile of model test area: (a) model test using plug body of circular column shape; (b) model test using plug body of circular truncated cone shape

Although the cross section of TTA is half-circular-half-rectangular shape according to the prototype, the cross section of TTA model is simplified as circular shape because the model test primarily focuses on the purposes of mechanism research and design concept recommendations. Altogether two models with different longitudinal shapes are made. One is circular column model with identical cross section area at both front and back faces. The other one is circular truncated cone model with larger cross section area on the back face and smaller cross section area on the front face. By taking into account the factors, including rock mass quality, rock wall thickness, jack output, and installation condition, dimensions of two TTA model are determined. For circular column model, its diameter is 38.5 cm and its length is 77 cm. For circular truncated cone model, its diameter is 35 cm on the front face and 42 cm on the back face, and its length is 77 cm. The contact areas between the plug body and the surrounding rock mass for these two models are both 9313 cm^2, so the anti-pulling capacity of them can be directly compared.

The rock wall between the parallel openings is firstly excavated to provide space for pouring of plug bodies. Cut blasting, static blasting and hand-hammer drilling methods are all used to achieve a satisfactory excavation effect. A concrete clan C30 was used for the plug body. Before model test, strength of concrete was evaluated by uniaxial compressive test. Three cubic concrete specimens with dimensions of 15 cm × 15 cm × 15 cm were prepared. The mean compressive strength of plug body material was 34.2 MPa.

2.3 Loading apparatus

The spot of model test area is shown in Fig. 2. The plug body of circular column model uses one jack with capacity of 5000 kN pushing force. The circular truncated cone model has used one jack with capacity of 5000 kN pushing force at earlier stage but fails to achieve surrounding rock mass failure. Therefore the loading apparatus was replaced by four jacks each with capacity of 3200 kN pushing force. The angle of inclination of the pushing forces for both models is 40°, which is same with the prototype.

2.4 Measurement layout

In order to capture the structural response of both TTA model and surrounding rock mass during loading process, a series of measurement approaches, including strain gauges, multi-point

(a)

(b)

Fig. 2 Spot of model test area: (a) rigid columns for circular truncated cone and circular column at earlier stage of model test; (b) replaced rigid column for circular truncated cone extensometers and dial gauges, are adopted. The strain gauges, denoted with a prefix YB (Fig. 3), are placed both inside the plug bodies and on the interfaces between the plug bodies and the surrounding rock mass, so as to monitor the strain distribution of the plug body and its interaction

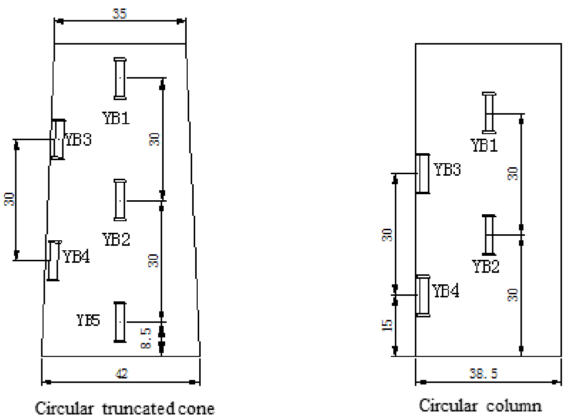

Fig. 3 Layout of strain gauges

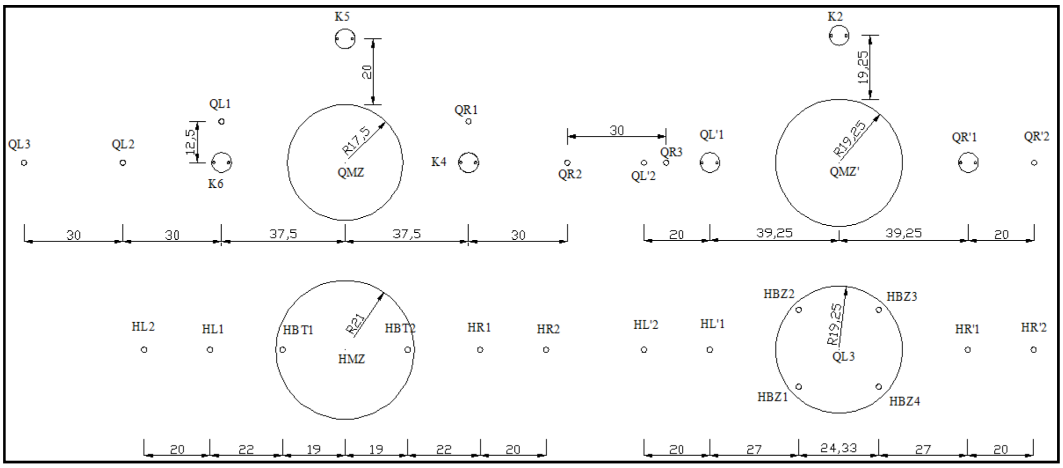

Fig. 4 Layout of strain gauges

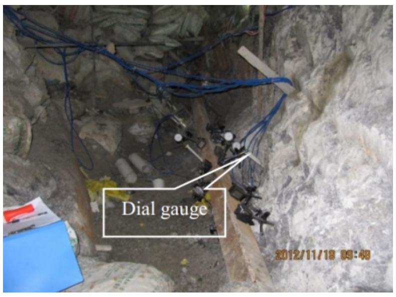

Fig. 5 Layout of dial gauges

characteristics with the surrounding rock mass. The multi-point extensometers, denoted with a prefix K (Fig. 4), are installed inside the drill holes of the surrounding rock mass around the plug bodies, so as to monitor the internal deformation distribution of the rock mass. The dial gauges, denoted with prefixes QL, QR, HL or HR (Figs. 4~5), are probing on the surface of the plug bodies and the surrounding rock mass with one ends, while the other ends are fixed on an I-shape steel placed on both sides of the rock wall, so as to monitor the surface deformation of the rock mass.

2.5 Model test process

The pushing forces are imposed on the back faces of the plug bodies. The load is increased step by step until failure occurs. For each stage of loading, the imposed load remains stable for 20 minutes and then increases to next stage. When failure occurs, the load stops increasing and gradually decreases to zero, thus the process constitutes a full loading-unloading cycle. The failure refers to either the interface slip failure between the plug bodies and the surrounding rock mass or the material failure of surrounding rock mass.

2.6 Result analysis

2.6.1Circular column model

The load gradually increased and the interface slip failure occurred when the imposed load reached 2460 kN. The monitored strain variation curves of plug body during loading process are given in Fig. 6. The surface deformation variation curves of the plug body and the surrounding rock mass during test are given in Figs. 7~8. By analyzing the curves given in Figs. 6~8, the following observations can be done.

(1) The monitoring data of strain gauges indicates that the magnitude of strain of plug body becomes larger as its back face approaches, and becomes smaller as the its back face recedes. Of the obtained data, the maximum strain is -0.000492 ε (negative value refers to compressive effect and positive value refers to tensile effect) and the minimum strain is -0.00008 ε. The strain distribution shows that the imposed load is transferred from the back face of the plug body to its front face and the variation extent of strain magnitude inside the plug body is considerable.

(2) It is analyzed from the monitoring data collected by multi-point extensometers and dial gauges that for the plug body and the surrounding rock mass, no remarkable irreversible deformation occurs. Brittle failure occurs on interfaces between the plug body and the surrounding rock mass. As the imposed load is gradually removed after failure occurs, spring back deformation occurs at the plug body and a large hysteresis loop curve forms. The plug body deforms much larger than the surrounding rock mass. The deformation of the back face corresponding to peak imposed load is 0.000349 m, and that of the front face is 0.000105 m. The magnitude of deformation of surrounding rock mass on back face is overall not considerable and ranges from 0.00003 m to 0.00009 m. The magnitude on front face is even smaller and ranges from 0.00001 m to 0.000014 m. For dial gauges on front face placed 59 cm and more distant from the plug body, numerical readings all remain zero. The distribution characteristics indicate that under imposed loading effect, the strength of interface between the plug body and the surrounding rock mass plays a decisive role.

(3) It is observed that the failure occurs on the interface between the plug body and the

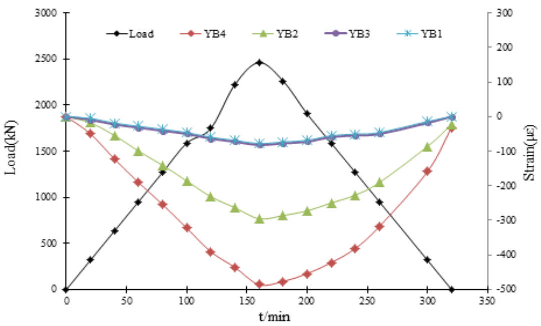

Fig. 6 Strain magnitude curves inside the plug body of circular column shape: the horizontal coordinate denotes duration of model test

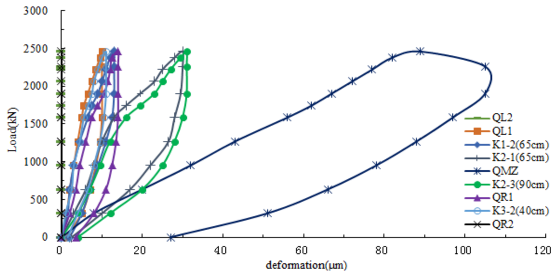

Fig. 7 Imposed load versus deformation curves for dial gauges and multi-point extensometers on the front face

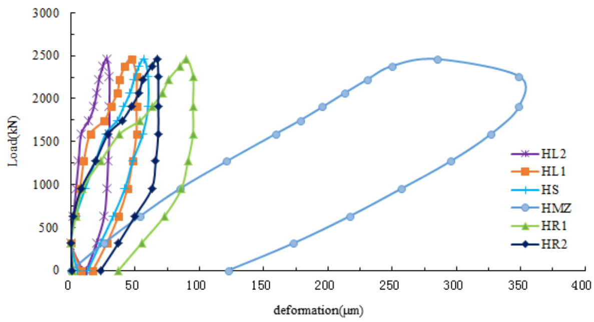

Fig. 8 Imposed load versus deformation curves for dial gauges and multi-point extensometers on the back face

surrounding rock mass. Rock mass itself remains undamaged. The failure characteristics of the interface is similar with the characteristics observed in bearing tests of pile foundations and direct shear tests of interfaces between concrete and rock. Meanwhile, the monitoring data of strain and deformation indicates that the deformation distribution law on front face of plug body is different from that on back face. It can be inferred that the failure of interface initiates on the back face side and then gradually expands to the front face side.

(4) Although rock wall drilling inevitably generate rough excavation surfaces to a certain extent, the anti-sliding effect provided by interface roughness is slight and can be neglected. The general frictional resistance stress can be calculated by averaging the imposed load on the interface area. The lateral area of circular plug body is 9313 cm^2 and the imposed load is 2460 kN when failure occurs. Therefore, the frictional resistance stress is 2.6 MPa.

2.6.2 Circular truncated cone model: First test

At earlier stage of model test, one jack with capacity of 5000 kN pushing force was used to conduct a full load-unloading cycle test. No failure occurs when the jack reaches its maximum value. The monitoring data obtained by strain gauges is shown in Fig. 9. The monitoring data obtained by multi-point extensometers and dial gauges are shown in Figs. 10-12.

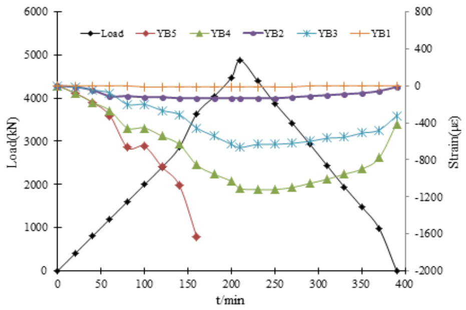

Fig. 9 Strain magnitude curves inside the plug body of circular truncated cone shape: the first test and the horizontal coordinate denotes duration of model test

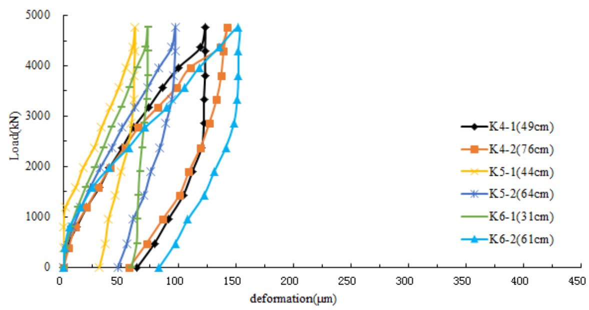

Fig. 10 Imposed load versus deformation curves for multi-point extensometers: the first test

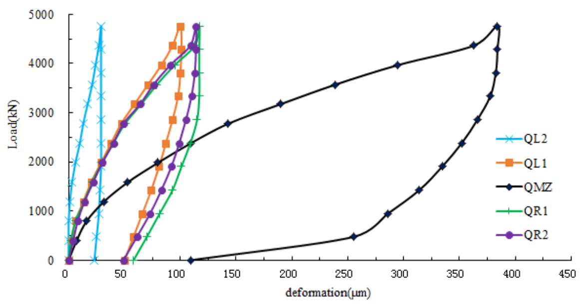

Fig. 11 Imposed load versus deformation curves for dial gauges on the front face: the first test

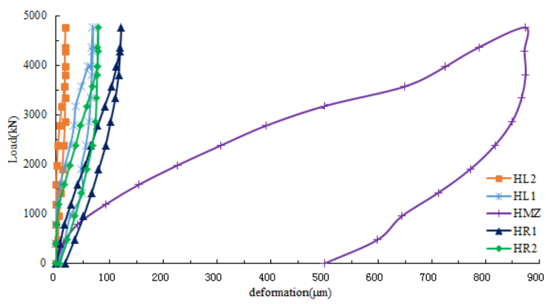

Fig. 12 Imposed load versus deformation curves for dial gauges on the back face: the first test

By analyzing the curves given in Figs. 9~12. The following observations can be done.

(1) The monitoring data of strain gauges indicates that strain magnitude of the plug body becomes larger as its back face approaches, and becomes smaller as its back face recedes. Of the strain gauges, YB5 reading exceeds its measurement range. The measured maximum reading is -0.0016 ε and the minimum is -0.00008 ε. The strain distribution shows that the imposed load is transferred from the back face of plug body to its front face, and the variation of strain magnitude inside the plug body is considerable.

(2) The maximum deformation of the front face of the plug body is -0.000384 m and that of the back face is -0.000875 m, according to the dial gauges. The deformation of surrounding rock mass on the back face side of rock wall is smaller than that on the front face side.

2.6.3 Circular truncated cone model: *Second test*

As no failure occurs in the first test, it is concluded that the plug body of circular truncated cone shape possesses higher bearing capacity. So the loading apparatus is replaced by four jacks each with capacity of 3200 kN pushing force. The second test still conducts a full loading-unloading cycle. When the imposed load reaches 11175 kN, brittle and broken sounds are heard and fractures are generated on the surrounding rock mass surfaces. Rock rupture and collapse are

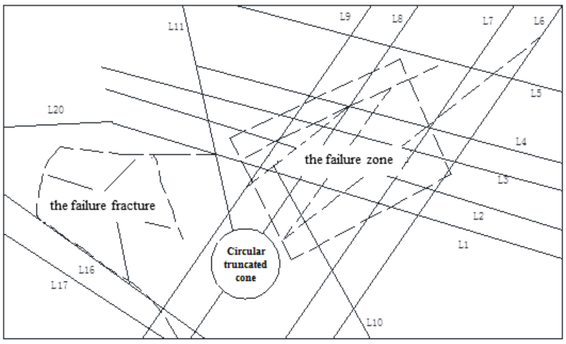

Fig. 13 Sketch map of local failure areas on the front face of surrounding rock mass

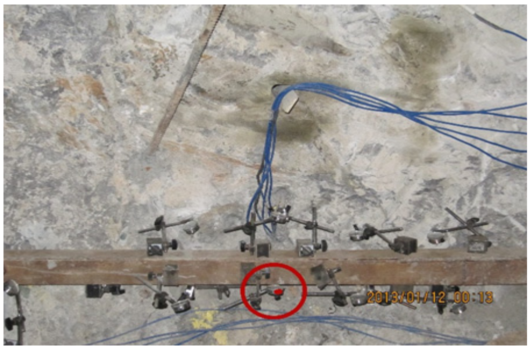

Fig. 14 Field image of the front face before failure occurs: the red circle denotes the location of the front side of the plug body

Fig. 15 Field image of the front face when failure occurs: the red rectangular denotes failure area of the rock mass

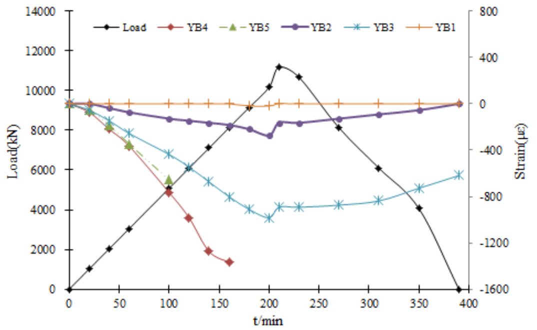

Fig. 16 Strain magnitude curves inside the plug body of circular truncated cone shape: the second test and the horizontal coordinate denotes duration of model test

also observed on top-left area of the front face (Figs. 13~15). The monitoring data are given by Figs. 16~19. It is shown that failure occurs for the surrounding rock mass.

By analyzing the curves given in Figs. 13~19, the following observations can be done.

(1) Of the strain gauges which are placed inside the plug body, two gauges nearest to the back face fails to record any data, thus the maximum strain magnitude cannot be obtained. Of the rest strain gauges, compared to the data collected in the first test, the data magnitudes are all larger, showing that the plug body can support larger load.

(2) At the preliminary stage of the loading process, the monitoring data shows linear growth trend, indicating that the surrounding rock mass is also at linear elastic deformation stage. When the impose load exceeds 7111 kN, the curve of imposed load and deformation begins to show non-linear increase trend. The deformation curve gradually turns into upper-convex shape and an inflection point appears. With the increase of deformation rate, the rock mass enters into elasto-plastic deformation stage. With continuous increase of imposed load, the deformation rate increases further. When the imposed load reaches 11175 kN, rock rupture is observed at the top-left area on the front face. At this point, the loading stage stops and the unloading stage begins.

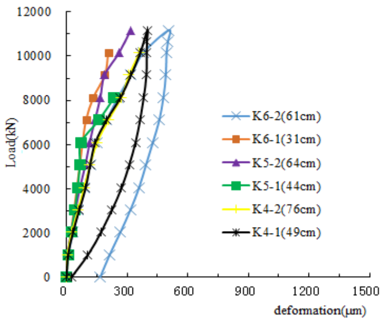

Fig. 17 Imposed load versus deformation curves for multi-point extensometers: the second test

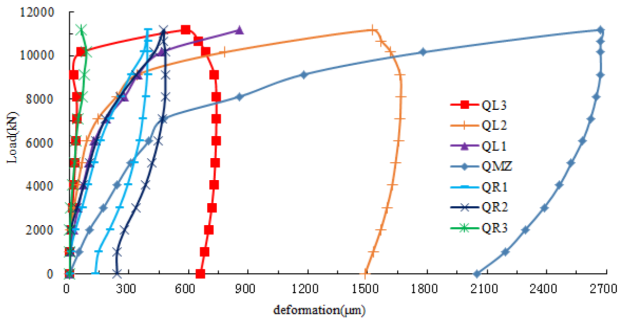

Fig. 18 Imposed load versus deformation curves for dial gauges on the front face: the second test

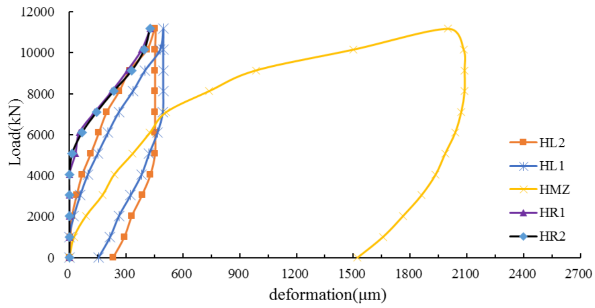

Fig. 19 Imposed load versus deformation curves for dial gauges on the back face: the second test

(3) The failure characteristics of surrounding rock mass is observed and recorded in detail. Two sets of dip-angled fractures intersect the excavation surfaces of the branch openings. The intersection cuts rock mass and generates blocks. Under high magnitude of imposed load, the top-left rock mass ruptures. Unloading process begins after rock rupture occurs. When the imposed load decreases to zero, the deformation of the plug body and the surrounding rock mass, revealed by dial gauges, decrease to a certain extent, but considerable residual deformations remains.

(4) The deformation data of the plug body and the surrounding rock mass on the front face is larger than those on the back face. Further, large deformation magnitudes are monitored at wide range on the front face side, while on the back face side no large deformation occurs. This is because as the increase of imposed load, more or more load is transferred from the plug body to the surrounding rock mass through interface. As the plug body is truncated cone with larger area at the front face and smaller area at the back face, the load bearing area of surrounding rock mass gradually expands from the back face side to the front face side. The deformation trend is observed in wide range of the surrounding rock mass on front face side, thus causing fractures of surrounding rock mass open and rock blocks collapse.

(5) Compared to the results of circular column model test, the circular truncated cone model test results show that the model of circular truncated cone shape is able to associate with the surrounding rock mass to achieve larger bearing capacity, rather than solely relies on

the shear strength of interface between the surrounding rock mass and the plug body. The maximum imposed load at the elastic deformation stage of the plug body of the circular column model is 1587 kN, while that of the circular truncated cone model is 7111 kN, which is 4.48 times larger. The imposed load corresponding to failure state of the circular column is 2460 kN, while that of the circular truncated cone model is 11175 kN, which is 4.54 times larger. The considerable gap of bearing capacities between the two model tests indicate that the plug body of circular truncated cone shape possesses much larger capacity.

2.7 Understandings of model test results

Altogether, the plug bodies with different shapes, which are circular column model and circular truncated cone model, are adopted to support increasing load. Two different failure patterns are obtained. The gap of bearing capacity between these two models is considerable. Following points are summarized:

(1) The failure pattern for the circular column model is brittle failure of interface between the plug body and the surrounding rock mass. On the other hand, the circular truncated model shows remarkable irreversible deformation characteristics during loading process and its failure pattern is surrounding rock mass failure on the front face side of the plug body. Overall, the failure pattern and failure characteristics of two models are different.
(2) The bearing mechanism of the plug body with circular column shape is similar with that of the pile foundation. The shear strength of interface between the plug body and the surrounding rock mass determines the bearing capacity while the material strength of surrounding rock mass has little contribution. For the model of circular truncated cone shape, due to its larger front face and smaller back face characteristics, the imposed load on the plug body can be transferred to the surrounding rock mass, which helps to enhance the bearing capacity of the plug body.
(3) For plug body of circular truncated cone shape, it is shown from the deformation monitoring data that large magnitude of deformation only occurs on the front face side while no considerable deformation occurs on the back face side. Thus, it can be inferred that, the deformation distribution pattern inside the rock wall takes on a “trumpet” shape.

3. Numerical simulation

3.1 Purpose of numerical simulation

Due to site restrictions of the model test, only deformation distribution at the surface areas of surrounding rock mass can be comprehensively monitored. The deformation distribution inside surrounding rock mass still remains unclear and can be only roughly estimated by limited monitoring data. Therefore, numerical simulation tool is adopted here to provide an insight into the detailed deformation and failure evolution process of surrounding rock mass. The numerical simulation is based on in-situ model test and covers the whole loading and unloading process. The software FLAC^{3D} (Cundall 2008) is adopted to carry out numerical analysis.

3.2 Procedures and basic ideas of numerical simulation

The procedure of numerical analysis is summarized in Fig. 20. Generally, the listed procedure can be divided into three major parts.

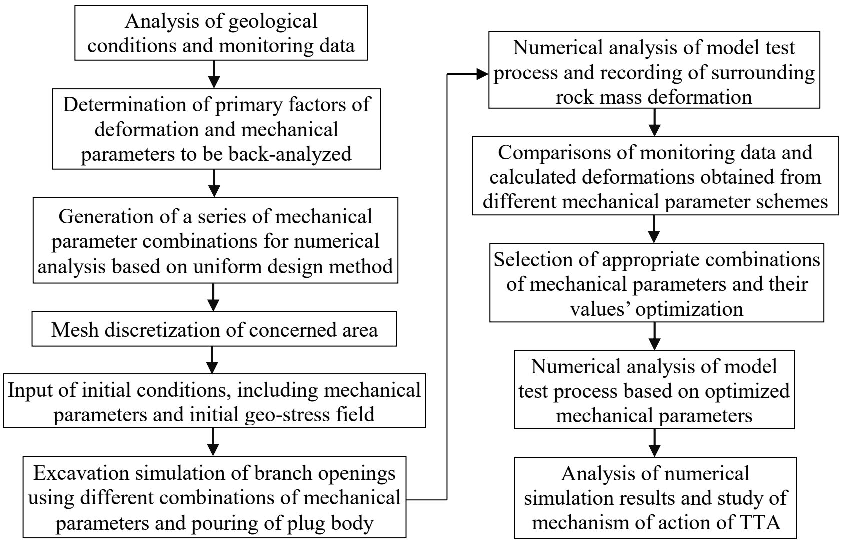

Fig. 20 Flowchart of numerical analysis

3.2.1 Determination of primary factors for surrounding rock mass deformation

The first part is to determine primary factors among mechanical parameters for surrounding rock mass deformation based on summary and analysis of geological conditions, monitoring data, and references from other projects with similar engineering backgrounds. Prior to model tests, rock mass mechanical properties were obtained by means of in-situ tests. Moreover, mechanical properties of rocks sampled from the field were also obtained indoor by means of laboratory experiments. The results show that, the measured values of deformation modulus, cohesion and frictional angle of rock mass are remarkably different from those of rock samples. The discrepancies of mechanical parameters obtained at the field and indoor can be largely attributed to the size effect of rock mass, which also characterizes the uncertainty of above three mechanical parameters. Therefore, in order to provide rational grounds for numerical analysis, the above three mechanical parameters are chosen as the primary factors and the objects to be back-analyzed.

3.2.2 Back-analysis of chosen mechanical parameters

The second part is the back-analysis of the chosen mechanical parameters. The uniform design method is adopted to generate a series of mechanical parameter combinations for numerical analysis. Field tests towards the rock mass recommends the range of mechanical parameters, as shown in Table 3. Based on uniform design concept, six combinations of deformation modulus, cohesion and frictional angle, as shown in Table 4, are given as input mechanical parameters for the back-analysis.

Table 3 Mechanical parameters of the rock mass

Rock mass	Deformation modulus E (GPa)	Cohesion C' (MPa)	Tangential (f') of frictional angle (°)
Limestone	30~55	1.0~3.5	1.0~2.0

Table 4 Combinations of chosen mechanical parameters based on uniform design method

No.	*E* (GPa)	*C*' (MPa)	*f*'	No.	*E* (GPa)	*C*' (MPa)	*f*'
1	30	1.5	1.4	4	45	1.0	1.8
2	35	2.5	2.0	5	50	2.0	1.0
3	40	3.5	1.2	6	55	3.0	1.6

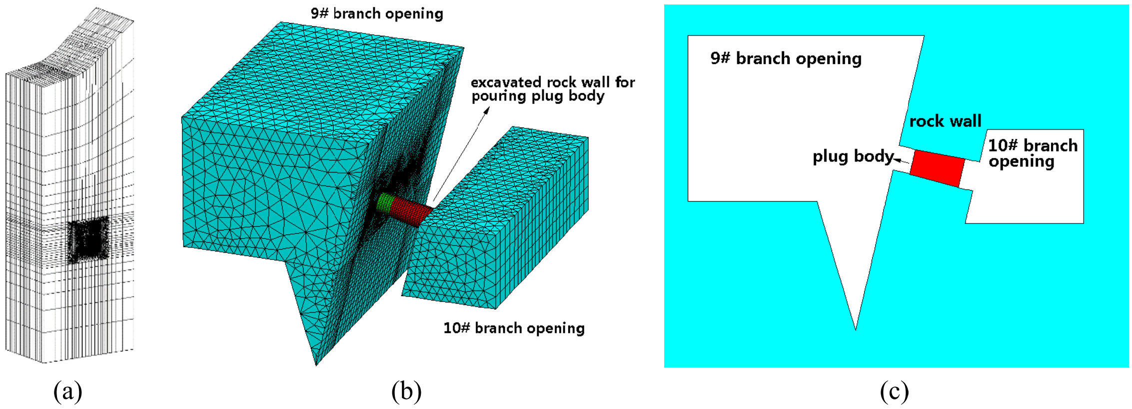

Fig. 21 Mesh for numerical simulation: (a) overall view; (b) excavation elements, including two branch openings and excavated rock wall for pouring plug body; (c) longitudinal section along the direction of imposed pushing force

Besides the generation of these parameters, other conditions are also required for the back-analysis. They are mesh discretization, initial geo-stress consideration, and simulation of necessary steps prior to model test. A three dimensional mesh covering the model test area is discretized and its excavation elements and typical section are shown in Fig. 21. The modelling range is 200 m × 200 m × 600 m (width × length × height). Totally there are 12345 nodes and 54321 elements. As the thickness of overburden rock mass at the model test area is not large, the initial geo-stress field is calculated based on overburden depth and Poisson's ratio of rock mass. Before the loads are imposed on the plug body, rock excavation and concrete pouring should be finished. Thus, numerical simulation of these steps is conducted accordingly.

By carrying out numerical calculations using the six combinations of mechanical parameters, six corresponding results are obtained. For each calculation, the process of model test is considered based on actual situations. The imposed load of model test is applied to the back face of the plug body. As the imposed load is gradually applied using 11 stages and then reaches its peak value 11175 kN, each numerical calculation also involves 11 stages of load applications. The obtained deformations of surrounding rock mass and the plug body are then compared to monitoring data derived from the field tests. It should be noted that, when the imposed load gradually increases to 11175 kN, local failures begin to occur around the surrounding rock mass near the plug body. In order to protect the loading apparatus, monitoring instruments and field personnel, the loading operation is stopped and unloading operation begins. For this loading stage, the imposed load does not remain stable for some time but is removed shortly after reaching 11175 kN. Therefore, the comparisons between monitoring data and numerical simulation results are conducted based on the results of 10th stage of imposed load.

Table 5 Finally adopted mechanical parameters for the rock mass

Deformation modulus (GPa)	Poisson's ratio	Cohesion (MPa)	Frictional angle (°)	Tensile strength (MPa)
45	0.25	3.5	58 (f' = 1.6)	2.0

Based on the comparisons, the combination of mechanical parameters that provides the most approximated solution is selected. By further adjustment proper values quantifying the mechanical properties of surrounding rock mass are obtained and deemed as the back-analysis results, as shown in Table 5.

3.2.3 Interpretation of model test based on calculation results

By using the back-analysis results of chosen mechanical parameters, numerical simulation is performed again. The third part is to interpret the mechanical and structural responses of surrounding rock mass based on the final numerical simulation results and to study the bearing mechanism of TTA.

3.3 Analysis of final numerical simulation results

3.3.1 Analysis of deformation distribution on the surfaces

Figs. 22~23 plot the deformation distributions corresponding to 10st stage of loading on the front face and the back face, respectively. Each figure puts the curves of monitoring data and calculation results together for comparison purpose. It is shown that, for both the front and the back faces, the calculation results and monitoring data are in good agreement and reveals identical deformation distribution law. As can be seen, the deformation of the plug body is considerably larger. Within certain range near the plug body, the surrounding rock mass also deforms remarkably.

3.3.2 Deformation evolution during loading process

The monitoring points on the plug body, denoted as QMZ and HMZ, and the monitoring points on surrounding rock mass on the front face side, denoted as QL1 and QR1, are chosen to plot their monitored deformation curves for comparison as shown in Fig. 24. It is indicated from the curves' comparison that, with the increase of imposed load, the deformation evolution curves plotted

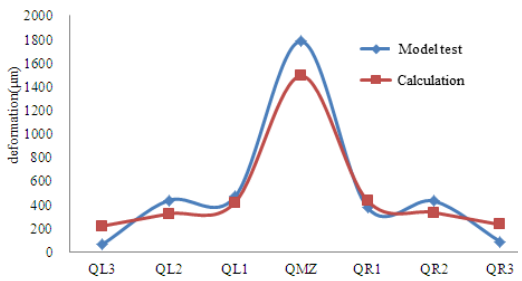

Fig. 22 Comparisons of surrounding rock mass deformations of monitoring data and numerical simulation results at the front face

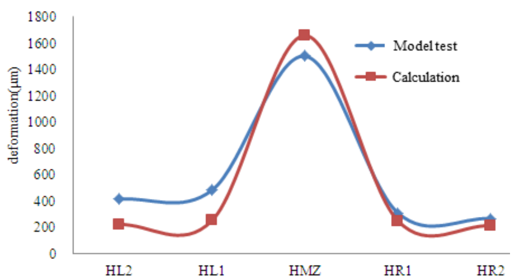

Fig. 23 Comparisons of surrounding rock mass deformations of monitoring data and numerical simulation results at the back face

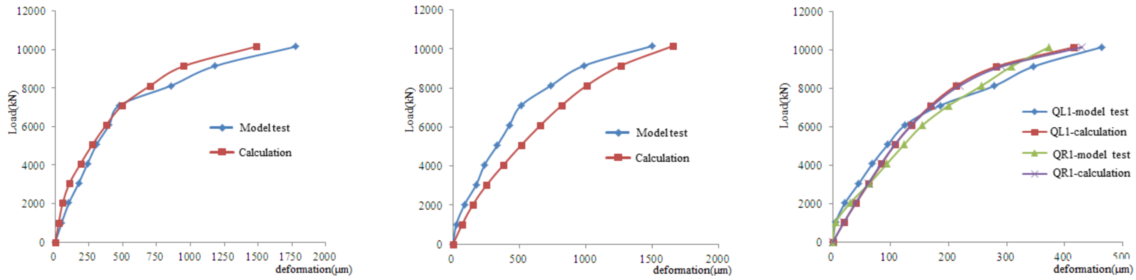

(a) (b) (c)

Fig. 24 Imposed load versus deformation curves: comparisons of monitoring data and numerical simulation results: (a) plug body on the front face side; (b) plug body on the back face side; (c) surrounding rock mass on the front face

based on numerical simulation exhibit consistent variation law with those curves plotted based monitoring data. The deformation magnitudes obtained by different approaches are also close. The agreement in both deformation evolution and deformation magnitude indicates that the reliability of numerical simulation and its capacity of reflecting the inherent mechanical and structural evolution process of model test. At initial stage of loading, deformation curves of all monitoring points exhibit linear elastic variation characteristics. When the imposed load increases to 7th stage and reaches the magnitude of 7111 kN on the back face of the plug body, the deformation curves exhibit non-linear variation trends and gradually turns into upper-convex shape. Inflection points also appear on the curves at the same time. The increase of imposed load leads to the increase of deformation rate, thus making the surrounding rock mass enter into elasto-plastic deformation stage.

3.3.3 Reliability of numerical simulation results and their further application

The above comparisons prove the reliability of the mechanical parameter back-analysis results and the effectiveness of numerical simulation approach for illustration and reflection of field model test. Thus, the numerical simulation results can be further utilized for studying the deformation distribution characteristics of the plug body and the surrounding rock mass at their internal areas that are difficult to access by monitoring instruments. Moreover, based on fully understanding the overall deformation distribution characteristics and combining other indexes provided by numerical simulation results, the bearing mechanism of TTA can be studied on a rational basis.

4. Interpretation of bearing mechanism of TTA

4.1 Evolution process of major calculation indexes

Deformation and equivalent plastic strain are used as major calculation indexes for interpreting the bearing mechanism of TTA.

The deformation contours and deformation vectors along the longitudinal section of the plug body under different stages of imposed loads are plotted in Fig. 25. The following remarks can be done. By observing the variation processes of deformation gnitudes and deformation vectors.

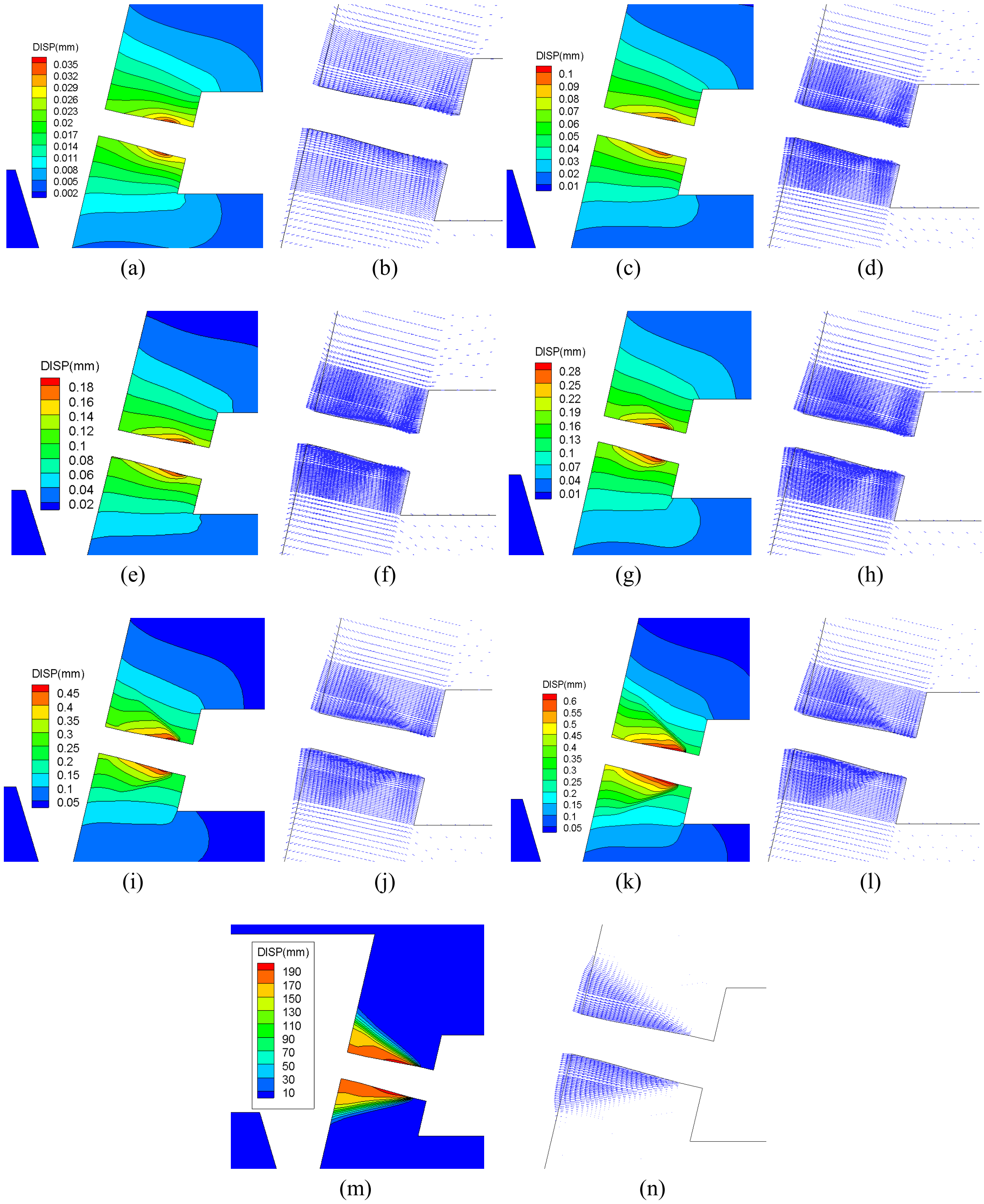

Fig. 25 Deformation contours and deformation vectors along the longitudinal section of plug body under different stages of imposed loads. (a),(c),(e),(g),(i),(k),(m): deformation contours under 1st, 3rd, 5th, 7th, 9th, 10th, and 11th stage of load, respectively; (b),(d),(f),(h),(j),(l),(n): deformation vectors under 1st, 3rd, 5th, 7th, 9th, 10th, and 11th stage of load, respectively

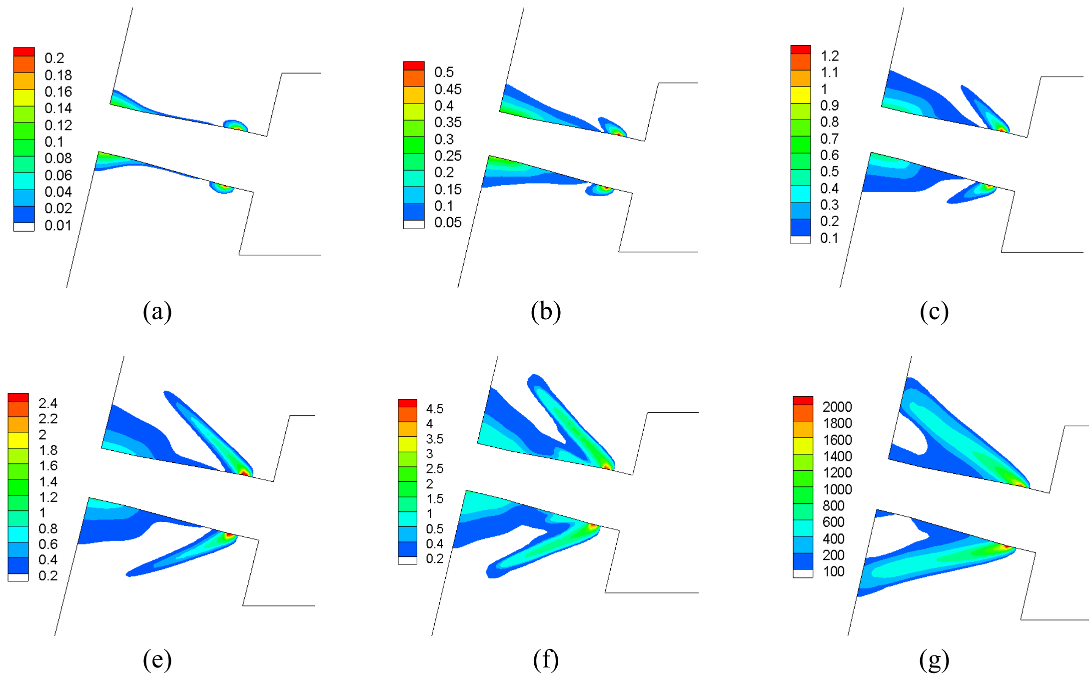

Fig. 26 Equivalent plastic strain contours along the longitudinal section of plug body under different stages of imposed loads: the unit is 0.001. (a) 1st stage of load; (b) 3rd stage of load; (c) 5th stage of load; (d) 7th stage of load; (e) 9th stage of load; (f) 11th stage of load

(1) The deformation vectors of surrounding rock mass under all stages of imposed loads are generally consistent with the loading direction.
(2) At the initial stage of loading, deformation gradients of surrounding rock mass are not large and the deformation contours distribute uniformly. The maximum deformation appears at the area near the back face of the plug body.
(3) With the increase of imposed load, deformation contours of surrounding rock mass gradually change and turn into a "trumpet" shape. For the final stage of loading, the numerical calculation fails to achieve convergence and the calculated deformation keeps increasing. Therefore the calculation for 11th stage of loading is forced to stop when large deformation is calculated.

The equivalent plastic strain contours along the longitudinal section of the plug body under different stages of imposed loads are plotted in Fig. 26. It is observed that, with the increase of imposed loads, a more and more remarkable "shear-belt" occurs in rock mass surrounding the plug body. Moreover, the development law of equivalent plastic strain contours is consistent with that of deformation contours. Based on the simulation results, it can be deduced that, if the imposed load is further increased, then the plug body and adjacent rock mass would be pushed out following a trumpet shape. As large deformation and considerable equivalent plastic strain are both observed at the surface area of surrounding rock mass around the plug body on the front face side, it is concluded that rock mass failure is most likely to occur at this area. The conclusions based on numerical simulation are consistent with the model test observations, indicating once again that the above numerical simulation results are rational.

4.2 Bearing mechanism of TTA

Based on the above observations, the bearing mechanism of TTA can be summarized as follows.

(1) TTA bearing mechanism. The bearing capacity of TTA is jointly provided by the shear resistance of interface between the plug body and the surrounding rock mass, and the shear resistance of surrounding rock mass itself. For plug body with circular column shape, its bearing capacity is very limited because the imposed loads cannot be effectively transferred to the surrounding rock mass. For plug body of circular truncated cone shape, it is able to take advantage of the material strength of surrounding rock mass, thus greatly enhancing its bearing capacity. Given the considerable gap of bearing capacities between different shapes of plug body, it is concluded that for TTA of circular truncated cone shape, the resistance provided by rock mass material accounts for a major proportion.

(2) The ultimate bearing capacity of TTA. Based on numerical simulation results, when calculation fails to achieve convergence, shear yield zone covers the surrounding rock mass area near the plug body. Moreover, the calculation enters into plastic flow stage as the magnitudes of deformation and equivalent plastic strain keep increasing. Therefore, it is concluded that the ultimate bearing capacity of TTA with circular truncated cone shape is determined by material strength of surrounding rock mass, while that of TTA with circular column shape is determined by interface strength between the plug body and the surrounding rock mass.

5. Recommendations for TTA design

By analyzing the model tests' results, and numerical simulation results, three recommendations are proposed for TTA design.

5.1 Shape selection of plug body.

As the circular truncated cone shape provides much larger bearing capacity, it is recommended this shape should be the first choice for TTA design. As for actual projects, half-circular-half-rectangular cross sections are more popular, it is further stated that, as a more general recommendation, the cross sections of the plug body should be designed with gradually smaller cross section area along the loading direction. This recommendation shares a same opinion with the experiences drawn from engineering practices, but it is established on a more persuasive basis.

5.2 Measures to enhance the bearing capacity of TTA.

As the material strength of surrounding rock mass around the plug body determines the ultimate bearing capacity of TTA, it is recommended that proper reinforcement measures can be taken to enhance the integrity and the stiffness of surrounding rock mass. Moreover, both the model test and numerical simulation results reveal that the failure zone of surrounding rock mass follows the trumpet-shape distribution. Therefore, reinforcement measures can be considered more accurately. For instance, cement grouting and anchorage support are effective ways to improve the performance of fractured surrounding rock mass. Once the quality of rock mass is favorable after proper reinforcement measures, the use of TTA will be more adaptive and flexible for various geological conditions.

5.3 Inclusion of rock mass strength

Currently, although TTA is widely adopted in engineering practices, its design still exclude the contribution of surrounding rock mass, thus leading to much conservative design plans and higher expense. Based on the above conclusions, the inclusion of rock mass strength factor into TTA design is rational and very promising. It is recommended that the role of surrounding rock mass should be properly considered to reflect the realistic bearing conditions of TTA.

6. Conclusions

This paper studies the bearing mechanism of TTA for suspension bridges using model test and numerical simulation approaches. Following conclusions are obtained.

- Model tests are carrying out using two different types of plug bodies of TTA. Test results show that the plug body of circular truncated cone shape possesses much larger bearing capacity than that of circular column shape. For the plug body of circular column shape, its bearing capacity is controlled by the interface strength between the plug body and the surrounding rock mass. The surrounding rock mass remains intact at peak load and no residual deformation occurs after unloading. For the plug boy of circular truncated cone shape, its bearing capacity is controlled by the material strength of surrounding rock mass. Failure of surrounding rock mass occurs at peak load and considerable residual deformation remains after unloading.
- Numerical simulation is adopted to understand the structural and mechanical responses of the plug body and the surrounding rock mass under imposed loads. Mechanical parameters of surrounding rock mass are firstly back-analyzed. The laws of deformation distribution and equivalent plastic strain distribution derived from numerical simulation results are in good agreement with the measurement results and observations at the field, indicating that the numerical simulation results are rational and can be further used to study the bearing mechanism of TTA.
- Based on the numerical simulation results, the bearing mechanism of TTA its ultimate bearing capacity is studied. It is discovered that the plug body of circular truncated cone shape is able to take advantage of the material strength of surrounding rock mass, which greatly enhances its bearing capacity. The ultimate bearing capacity of TTA, therefore, is determined by the material strength of surrounding rock mass.
- Recommendations for TTA design, in terms of shape selection of the plug body, measures to enhance the bearing capacity, and inclusion of rock mass strength, are discussed and given based on the obtained conclusions.

Acknowledgments

This study was supported by the National Natural Science Foundation of China (Nos. 51409013, 51539002) and the Basic Research Fund for Central Research Institutes of Public Causes (Nos. CKSF2014066/YT, CKSF2017014/YT). These supports are greatly acknowledged and appreciated.

References

Ammann, O.H. (1933), "George Washington Bridge: General conception and development of design", *Transact. Am. Soc. Civil Engrs..*, **97**(1), 1-65.

Bencardino, F. and Condello, A. (2014), "Experimental study and numerical investigation of behavior of RC beams strengthened with steel reinforced grout", *Comput. Concrete, Int. J.*, **14**(6), 711-725.

Bencardino, F. and Condello, A. (2015), "SRG/SRP-concrete bond-slip laws for externally strengthened RC beams", *Compos. Struct.*, **132**, 804-815.

Bildik, S. and Laman, M. (2015), "Experimental investigation of the effects of pipe location on the bearing capacity", *Geomech. Eng., Int. J.*, **8**(2), 221-235.

Chen, H., Xia, C. and Li, R. (1995), "Stability analysis of the rock mass in the east anchoring area of Guangdong Humenbridge", *J. Tongji Univ.*, **23**(3), 338-342.

Cundall, P.A. (2008), *FLAC3D Manual: A Computer Program for Fast Lagrangian Analysis of Continua* (Version 4.0), Itasca Consulting Group, Inc., Minneapolis, MN, USA.

Hataf, N. and Shafaghat, A. (2015), "Numerical comparison of bearing capacity of tapered pile groups using 3D FEM", *Geomech. Eng., Int. J.*, **9**(5), 547-567.

Hu, B., Zeng, Q., Rao, D., Wang, S., Peng, Y., Liu, B., Liu, H. and Zhao, H. (2007), "Study on deformation law and failure mechanism of anchorage-surrounding rock system under tensile-shear complex stresses", *Chinese J. Rock Mech. Eng.*, **26**(4), 712-719.

Kame, G.S., Dewaikar, D.M. and Choudhury, D. (2012), "Pullout capacity of vertical plate anchors in cohesion-less soil", *Geomech. Eng., Int. J.*, **4**(2), 105-120.

Lei, Z.H. (2005), "Construction techniques for anchorages of Jiaolongba bridge on No.214 National Road", *World Bridges*, **2**, 27-29.

Lu, Y.C. (2003), "The east tunnel-anchor of Chongqing Egongyan Yangtze River bridge", *China Municip. Eng.*, **6**, 31-34.

Miki, C., Homma, K. and Tominaga, T. (2002), "High strength and high performance steels and their use in bridge structures", *J. Construct. Steel Res.*, **58**(1), 3-20.

Min, X., Yang, M. and Wang, K. (2011), "Study on construction technology of tunnel-type anchorage of suspension bridge", *Copper Eng.*, **62**(5), 839-849.

Moradi, G. and Abbasnejad, A. (2015), "Experimental and numerical investigation of arching effect in sand using modified Mohr Coulomb", *Geomech. Eng., Int. J.*, **8**(6), 829-844.

Niroumand, H. and Kassim, K.A. (2013), "A review on uplift response of symmetrical anchor plates embedded in reinforced sand", *Geomech. Eng., Int. J.*, **5**(3), 187-194.

Roberts, G., Anderson, J.K., Hamilton, J.A.K., Henderson, W., McNeil, J.S., Roberts, G. and Shirley-Smith, H. (1967), "Forth road bridge", *Proceedings of the Institution of Civil Engineers*, **32**(3), 321-512.

Saleem, M. (2015), "Application of numerical simulation for the analysis and interpretation of pile-anchor system failure", *Geomech. Eng., Int. J.*, **9**(6), 689-707.

Shen, R.F., Leung, C.F. and Chow, Y.K. (2013), "Physical and numerical modeling of drag load development on a model end-bearing pile", *Geomech. Eng., Int. J.*, **5**(3), 195-221.

Spadea, G., Bencardino, F., Sorrenti, F. and Swamy, R.N. (2015), "Structural effectiveness of FRP materials in strengthening RC beams", *Eng. Struct.*, **99**, 631-641.

The Professional Standards Compilation Group of the People's Republic of China (2002), Design Specification for Highway Suspension Bridge (draft standard for approval); China Communications Press, Beijing, China.

The Professional Standards Compilation Group of the People's Republic of China (2015), Standard for Engineering Classification of Rock Mass; China Communications Press, Beijing, China.

Wang, Y. and Cao, H. (2004), "Construction techniques of tunnel-type anchorage for suspension bridge", *Bridge Construct.*, **2**, 53-55.

Wang, H., Gao, B. and Sun, Z. (2005), "Study on mechanical behavior of tunnel anchorage system for suspension bridge", *Chinese J. Rock Mech. Eng.*, **24**(15), 2728-2735.

Wang, J., Liu, W., Wang, L. and Han, X. (2015), "Estimation of main cable tension force of suspension bridges based on ambient vibration frequency measurements", *Struct. Eng. Mech., Int. J.*, **56**(6), 939-957.

Xia, C., Chen, H. and Li, R. (1997), "Testing study on field structure model of the east anchorage of Guangdong Humenbridge", *Chinese J. Rock Mech. Eng.*, **16**(6), 571-576.

Xiao, B., Wu, X. and Peng, C. (2005), "Stability of the anchorage wall rock of tunnel for Chongqing Egongyan bridge", *Chinese J. Rock Mech. Eng.*, **24**(5), 591-595.

Yang, J., Guo, Z. and Wan, R. (2002), "Application of tunnel anchorage with anchor rods to anchor system of the Second Yangtze River bridge in Wanzhou city", *Highway*, **1**, 40-43.

Zhang, Q., Hu, J., Chen, G., Liao, J., Zhang, Y. and Bian, Z. (2012), "Study of rock foundation stability of Aizhai Bridge", *Chinese J. Rock Mech. Eng.*, **31**(12), 2420-2430.

Zhang, W., Ge, Y. and Levitan, M. L. (2013), "A method for nonlinear aerostatic stability analysis of long-span suspension bridges under yaw wind", *Wind Struct., Int. J.*, **17**(5), 553-564.

Zhang, X., Li, Q., Ma, Y., Zhang, X. and Yang, S. (2014), "Large-scale pilot test study on bearing capacity of sea-crossing bridge main pier pile foundations", *Geomech. Eng., Int. J.*, **7**(2), 201-212.

Zhu, J., Wu, A. and Huang, Z. (2006), "Pulling test of anchorage model of Siduhe suspension bridge", *J. Yangtze River Sci. Res. Inst.*, **23**(4), 51-55.

Zhu, H., Mei, G., Xu, M., Liu, Y. and Yin, J. (2014), "Experimental and numerical investigation of uplift behavior of umbrella-shaped ground anchor", *Geomech. Eng., Int. J.*, **7**(2), 165-181.

CC